1
From Magnetic Mirrors to Atom Chips[1)]

Andrei Sidorov and Peter Hannaford

1.1
Introduction

Following the advent of laser cooling and trapping techniques in the 1980s, a new exciting area of research, 'atom chips', has emerged in which sophisticated micron-scale structures on planar substrates are produced utilizing the latest technological developments in lithography and nanofabrication. These complex microstructures produce tiny magnetic field configurations which can trap, cool, and manipulate ensembles of ultra-cold atoms in the vicinity of a surface. Scaling down the dimensions of atom trapping geometry offers extended possibilities for the production and control of Bose–Einstein condensates (BECs). Enormous progress on the generation of BECs and quantum degenerate Fermi gases, on-chip matter–wave interferometers, and integrated detectors has been made in the last few years.

In the second section of this article we trace the historical evolution of this new field, from the first surface-based atom optical elements – magnetic mirrors – to the present-day micro-fabricated structures on a substrate – atom chips. In Section 1.3 we present the basic principles of magnetic mirrors for cold atoms and describe different types of magnetic mirror. Section 1.4 describes the production of a BEC on a permanent magnetic film atom chip; the application of this atom chip to probe the topology of magnetic fields using RF spectroscopy and to study the adiabatic splitting of a BEC in a double well for sensing asymmetric potentials; and investigations of the spatially dependent relative phase evolution of a two-component BEC. Finally, in Section 1.5 we describe a permanent magnetic lattice on an atom chip for trapping and manipulating multiple arrays of ultra-cold atoms and quantum degenerate gases.

1) We dedicate this article to the memory of our friend and colleague Geoffrey I. Opat.

Atom Chips. Edited by Jakob Reichel and Vladan Vuletić

ISBN: 978-3-527-40755-2

1.2 Historical Background

In 1983 Opat [1] proposed the idea of using periodic arrays of electric fields on a planar substrate to reflect beams of polar molecules in a matter–wave interferometer. Almost a decade later the Melbourne group [2] reported the reflection of a beam of chloromethane (CH_3Cl) molecules from the exponentially decaying electric field above a periodic array of electrodes of alternating polarity.[2)] Opat and coworkers [3] then extended these ideas to periodic arrays of magnetic fields to create a surface-based mirror for reflecting beams of laser-cooled atoms (Figure 1.1a). As slowly moving atoms in positive (or 'low-field seeking') magnetic states approach the periodic magnetic structure they experience an exponentially increasing magnetic field, with decay length $a/2\pi$ (where a is the period), and for sufficiently large magnetic fields the atoms are repelled by the structure. A number of schemes [3] were proposed for producing the periodic magnetic structures, including the use of arrays of magnets of alternating polarity, periodic magnetic fields 'recorded' on ferromagnetic substrates as in sound recording, and planar arrays of parallel wires alternately carrying electric current in opposite directions. Methods for fabricating the surface-based microstructures were suggested including lithographical techniques used in the electronics industry.

The first magnetic mirror for cold atoms was realized in 1995 by Roach *et al*. [4] by recording sinusoidal signals onto a magnetic audio-tape and observing the retroflection of laser-cooled rubidium atoms from the recorded structure. Soon after, Sidorov *et al*. [5] in Melbourne reported the retroreflection of cold cesium atoms from a 2-mm-period planar array of Nd-Fe-B magnets of alternating polarity. In 1997 the Sussex group demonstrated the focusing and multiple reflection of cold atoms bouncing on a curved magnetic mirror made from a concave-shaped floppy disk or video tape [6, 7].

One of the major challenges was to be able to scale the magnetic structures down to micron-scale periods, in order to produce a hard mirror with very short decay length and minimal finite-size effects. This problem was basically solved when it was shown [8] that a grooved periodic magnetic structure produces a magnetic field distribution that is essentially the same as that above an array of magnets of alternating polarity. The Melbourne group subsequently demonstrated the specular reflection of cold atoms from a 1-μm-period magnetic mirror constructed from micro-fabricated grooved structures coated with perpendicularly magnetized film [9, 10]. The scaling down of the period to 1 μm represented a significant advance in the miniaturization of surface-based atom optical elements.

In 1999 the Melbourne [11] and Harvard/Orsay/Gaithersburg [12] groups reported a magnetic mirror for cold atoms constructed from a planar array of current-carrying conductors lithographically patterned on a silicon wafer or a sapphire sub-

2) The beam of slowly moving polar molecules was produced in a gravity-assisted molecular beam line experiment (GAMBLE).

strate. A feature of this type of magnetic mirror is that the magnetic field may be readily varied, switched or modulated by varying the current in the conductors. Such magnetic mirrors were the first micro-fabricated surface-based optical elements for cold atoms and represented a significant step towards the development of more sophisticated atom chips based on micro-fabricated current-carrying conductors on a substrate [13–15].

In an earlier paper, Weinstein and Libbrecht [16] at CalTech had proposed various planar current-carrying wire geometries for constructing microscopic electromagnetic traps for cold atoms including the use of superconducting wire structures. In 1998 Vuletić *et al*. [17] and Fortágh *et al*. [18] in Munich demonstrated 3D microtraps for cold atoms based on a combination of electromagnets and permanent magnets or current-carrying conductors, and Drndic *et al*. [19] at Harvard reported the fabrication of micro-electromagnetic traps with geometries proposed in [16]. In 1999 the Munich group [20] reported the use of surface magnetic microtraps based on a 'U'-shaped wire quadrupole microtrap and a 'Z'-shaped wire Ioffe–Pritchard (IP) microtrap, with non-zero potential minimum to eliminate spin-flip losses, for the trapping of cold atoms on a substrate. Soon after, other groups [21–24] demonstrated the guiding of laser-cooled atoms by current-carrying wires, and Davis [25] proposed the use of permanent magnetic structures as miniature waveguides to transport cold atoms on a substrate. In 2000 the Innsbruck group [26] reported the trapping and guiding of cold atoms using a micro-fabricated circuit on a substrate, which they called an 'atom chip'. In the following year the Munich group [27] demonstrated a magnetic conveyer belt for transporting and merging cold atoms on an atom chip.

A major breakthrough came at the International Conference on Laser Spectroscopy in Snowbird in 2001 when Hänsel *et al*. [28] from Munich and Ott *et al*. [29] from Tübingen simultaneously announced the realization of a Bose–Einstein condensate (BEC) of ^{87}Rb atoms in a current-carrying magnetic microtrap on an atom chip. The use of miniature magnetic microtraps allowed the scaling down of the electric currents required to produce a BEC and the scaling up of the trap confinement and elastic collision rate, thus greatly simplifying and speeding up the production of a BEC. In 2006 Aubin *et al*. ([30], Chapter 12) in Toronto realized a degenerate Fermi gas of ^{40}K atoms on an atom chip by sympathetic cooling with ultra-cold ^{87}Rb atoms.

One of the next big challenges was to see if it was possible to perform coherence or interference experiments on ultra-cold atoms trapped on an atom chip at distances close to the surface (Chapters 4 and 5). In 2004 Treutlein *et al*. [31] in Munich reported the coherent manipulation of two hyperfine states of ultra-cold ^{87}Rb atoms in a current-carrying magnetic microtrap, with coherence times exceeding 1 s. This opened the way for Ramsey interferometry and miniature atomic clocks on an atom chip ([32], Chapter 8). However, on-chip interferometry by spatially splitting the condensate proved to be more challenging owing to difficulties of phase preservation and control of the condensate. In 2005 the MIT/Harvard groups [33] dynamically split a condensate by deforming a single-well magnetic trap into a double-well potential, but non-adiabatic evolution in a quartic potential during the splitting

process led to an unpredictable relative phase. A major breakthrough came when the Heidelberg/Vienna group demonstrated a phase-preserving splitting scheme based on RF-induced adiabatic potentials ([34], Chapter 7), which allowed accurate control over the splitting process and the observation of reproducible interference fringes with a deterministic phase. In the same year the Boulder/Harvard groups [35] achieved splitting, reflection, and recombining of condensate atoms in a Michelson interferometer using a standing-wave light field in a waveguide on a chip. In 2007 the MIT/Harvard groups [36] reported the observation of phase coherence between two separated BECs on an atom chip for times up to about 200 ms after splitting the condensate. In 2009 the Munich group [37] demonstrated the coherent manipulation of BECs in a state-dependent potential with microwave fields on an atom chip, allowing the on-chip generation of multi-particle entanglement and quantum-enhanced metrology with spin-squeezed states [38] (Chapter 8).

Very recently, Deutsch *et al*. [39] in Paris have reported coherence times as long as 58 s in a Ramsey interferometer experiment on ^{87}Rb atoms trapped on an atom chip. The long coherence times are interpreted in terms of a spin self-rephasing mechanism induced by an identical spin rotation effect that occurs during collisons in the forward direction between two identical particles [40]

In parallel developments Sinclair *et al*. [41] in London produced a BEC on a permanent-magnet atom chip based on periodically magnetized videotape and Hall *et al*. [42, 43] in Melbourne produced a BEC in a microtrap on a TbGdFeCo permanent magnetic film atom chip. BECs have since been produced in microtraps on a Co-Cr-Pt hard disk [44] and on a Fe-Pt magnetic foil atom chip [45]. In 2007 Whitlock *et al*. in Amsterdam [46, 47] constructed a 2D asymmetric magnetic lattice with periods of 22 and 36 μm in orthogonal directions on a Fe-Pt film atom chip and the Melbourne group [48, 49] constructed a 1D 10-μm-period magnetic lattice on a TbGdFeCo film atom chip. Both groups demonstrated the loading of ultracold atoms into multiple sites of the permanent magnetic lattice. Magnetic lattices can be readily scaled to have a very large number of lattice sites and could form the basis of storage registers for quantum information processing.

Superconducting wires offer the prospect of an extremely low noise environment for trapped ultra-cold atoms. In 2006 Nirrengarten *et al*. ([50] and Chapter 10) in Paris reported the trapping of ultra-cold atoms on a superconducting atom chip and the following year Mukai *et al*. [51] in Tokyo demonstrated the trapping of atoms on a persistent supercurrent atom chip. In 2008 the Paris group [52] realized a BEC on a superconducting atom chip and the Tübingen group [53] demonstrated the Meissner effect using ultra-cold atoms trapped by a superconducting wire on an atom chip. The development of superconducting atom chips also opens the way to new fundamental quantum physics experiments such as the coupling of a BEC to superconducting loops [54].

Comprehensive review articles on magnetic mirrors, microtraps and atom chips for ultra-cold atoms and quantum degenerate gases have been published by Hinds and Hughes [55], Folman *et al*. [13], Reichel [14], and Fortágh and Zimmermann [15].

1.3
Magnetic Mirrors for Cold Atoms

1.3.1
Basic Principles

We first consider an atom with magnetic dipole moment $\boldsymbol{\mu}$ moving in an inhomogeneous magnetic field $\boldsymbol{B}(x, y, z)$. If the rate of change of the direction of $\boldsymbol{B}(x, y, z)$ as seen by the moving atom is slow compared with the atom's Larmor frequency, then the orientation of $\boldsymbol{\mu}$ can adiabatically follow the direction of the magnetic field and the position-dependent interaction potential $U_{\text{int}}(x, y, z) = -\boldsymbol{\mu} \cdot \boldsymbol{B}(x, y, z)$ exerts a gradient or Stern–Gerlach force on the atom given by $\boldsymbol{F}_{\text{grad}} = \nabla(\boldsymbol{\mu} \cdot \boldsymbol{B}) = -m_{\text{F}} g_{\text{F}} \mu_{\text{B}} \nabla B(x, y, z)$, where m_{F} is the magnetic quantum number, g_{F} the Landé factor, and μ_{B} the Bohr magneton. Thus, atoms oriented in positive (or low-field seeking) magnetic states ($m_{\text{F}} g_{\text{F}} > 0$) experience a negative force and are repelled by an increasing magnetic field, while atoms in negative (or high-field seeking) magnetic states ($m_{\text{F}} g_{\text{F}} < 0$) are attracted by an increasing magnetic field.

We now consider the inhomogeneous magnetic field produced by a periodic array of magnets having alternating perpendicular magnetization $M(y, z) = +M_z$ and $-M_z$ in the y direction with period a (Figure 1.1a). For an *infinite* array of long, thick ($t \gg a/2\pi$) magnets of width $a/2$, the components and the magnitude of the magnetic field above the array are given by [5]

$$\begin{aligned} B_y(y, z) &= B_0 \mathrm{e}^{-kz} \left(\sin ky - 1/3 \mathrm{e}^{-2kz} \sin 3ky + \ldots \right) , \\ B_z(y, z) &= B_0 \mathrm{e}^{-kz} \left(\cos ky - 1/3 \mathrm{e}^{-2kz} \cos 3ky + \ldots \right) , \\ |B(y, z)| &= B_0 \mathrm{e}^{-kz} \left(1 - 1/3 \mathrm{e}^{-2kz} \cos 2ky + \ldots \right) , \end{aligned} \tag{1.1}$$

where $k = 2\pi/a$, and $B_0 = 8M_z$ (Gaussian units) is a characteristic surface magnetic field. For distances $z \gg a/4\pi$, Eq. (1.1) reduce to

$$\left[B_y(y, z);\ B_z(y, z) \right] \approx \left[B_0 \mathrm{e}^{-kz} \sin ky;\ B_0 \mathrm{e}^{-kz} \cos ky \right] , \quad |B| \approx B_0 \mathrm{e}^{-kz} . \tag{1.2}$$

Equation (1.2) indicates that for distances $z \gg a/4\pi$ the magnitude of the magnetic field is no longer dependent on y and falls off exponentially with distance z, with decay length $k^{-1} = a/2\pi$, while the direction of the magnetic field for a given distance z rotates in the yz-plane with period a as y varies (Figure 1.1a). Thus, an atom in a weak-field seeking magnetic state moving adiabatically towards the surface will be repelled by the exponentially increasing magnetic field, and if its magnetic potential energy exceeds the kinetic energy with which it approaches the surface the atom will be reflected. For a pure single-harmonic potential, Eq. (1.2) holds for all distances z above the array. For an array of magnets of finite thickness t, B_0 in Eq. (1.2) is replaced by $B_{\text{s}} = (1 - \mathrm{e}^{-kt}) B_0$ [10, 56]. The distance of

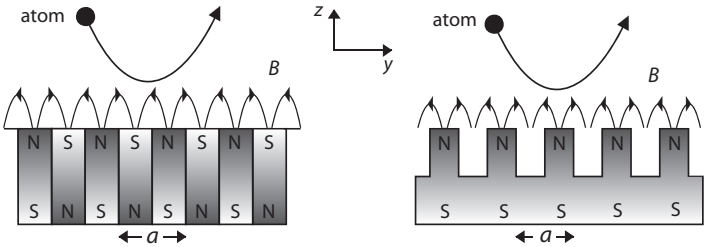

Figure 1.1 Schematic diagram of (a) a magnetic mirror consisting of perpendicularly magnetized elements of alternating polarity, (b) a grooved perpendicularly magnetized microstructure [10].

closest approach to the surface for an atom of mass M dropped from height h is $z_0 \approx (a/2\pi)\ln(m_F g_F \mu_B B_s/Mgh)$.

For small distances ($z < a/4\pi$) above the array, higher-order spatial harmonics in Eq. (1.1) contribute a corrugation, which have a relative amplitude given to good approximation by $C \approx 1/3(Mgh/m_F g_F \mu_B B_0)^2$ [56]. Such a corrugation leads to a diffusive component in the reflected atoms with an angular spread $\Delta\theta_{rms} \approx \sqrt{2}C$.

For a *finite* array of N magnets the magnetic field produced by the semi-infinite array of 'missing' magnets on the left (right) hand side of the mirror (Figure 1.1a) creates an effective magnetic field approximately the same as that of a magnet of width $a/4$ centered at $y = -Na/4$ $(+Na/4)$ [5]. Thus, by placing two magnets, with width $a/4$ and opposite magnetizations, one at each end of the array, the magnetic field above a large area of a finite array will mimic the field above an infinite array.

Typical magnetic fields required to reflect cold atoms dropped from a height $h = 20$ mm range from 47 G for cesium to 2.5 G for lithium. The reflecting potential for a magnetic mirror with a characteristic surface field of $B_0 = 4.2$ kG (thick Nd-Fe-B magnets) is 24 μeV (280 mK).

A magnetic mirror may be turned into a spatial diffraction grating, or a diffractive beam splitter, for slowly moving atoms by applying a uniform bias field B_{1z} (or B_{1y}) [3, 57]. For distances $z \gg a/4\pi$ above the array, the components of the magnetic field are given by expressions similar to Eq. (1.2) but with the addition of B_{1z} to the right-hand side of the B_z component. The magnitude of the magnetic field is then given by

$$|B(y,z)| \approx \left(B_{1z}^2 + 2B_{1z}B_0 e^{-kz}\cos ky + B_0^2 e^{-2kz}\right)^{1/2} . \tag{1.3}$$

The second term in Eq. (1.3) is periodic in y, and may act as a spatial diffraction grating, while the third (mirror) term dies away rapidly compared with the grating term. This leads to the periodic corrugated pattern in Figure 1.11d.

A magnetic mirror may also be converted into a temporal diffraction grating, or an 'acousto-optic modulator', for cold atoms by vibrating the magnetic structure or applying an oscillating orthogonal magnetic field [58].

1.3.2 Experimental Realization of Magnetic Mirrors

1.3.2.1 Macroscopic Array of Rare-Earth Magnets of Alternating Polarity

To test the basic principles of the magnetic mirror, we first constructed a planar periodic array of 18 1-mm-wide Nd-Fe-B magnets of alternating polarity, with a 0.5-mm-wide magnet at each end to compensate for end-effects [5]. Hall probe measurements indicate that the B_y and B_z components above the array exhibit a sine and cosine dependence on y, while the magnitude of the magnetic field shows an exponential dependence on z, given by Eq. (1.2), with $a = 2.06\,\text{mm}$ and $B_0 = 4.2\,\text{kG}$.

Time-of-flight (TOF) absorption measurements for laser-cooled cesium atoms optically pumped towards the $|F = 4, m_F = +4\rangle$ low field-seeking state and dropped from a height $h = 22\,\text{mm}$ onto the magnetic mirror exhibit two peaks (Figure 1.2). The first peak corresponds to atoms falling through the broad probe beam and the second peak, which was recorded with the probe beam turned on after the falling atoms had passed, corresponds to atoms reflected from the magnetic mirror. The relative intensities of the bounce and fall signals indicate a reflectivity close to 100 %. Similar measurements taken for atoms optically pumped towards the $|F = 4, m_F = -4\rangle$ high field-seeking state exhibit only weak reflection, confirming that the observed reflection is magnetic in origin. Studies of the spatial distribution of the incident and reflected atoms, by recording the transmission of a broad probe beam in a CCD array, indicate that the reflection is predominantly specular.

However, in order to produce a 'hard' magnetic mirror in which a cloud of atoms with a spread of velocities are all reflected from approximately the same plane, mag-

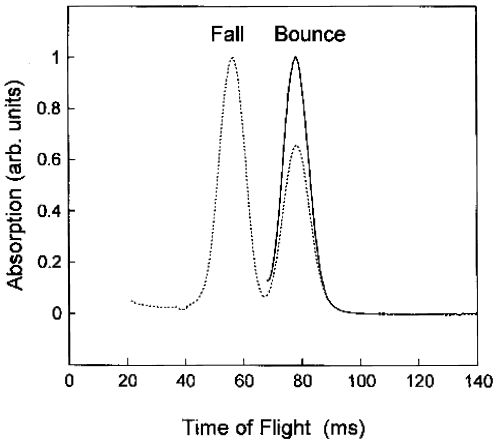

Figure 1.2 Time-of-flight absorption measurement showing the reflection of a beam of laser-cooled cesium atoms normally incident on a magnetic mirror constructed from a planar array of Nd-Fe-B magnets of alternating polarity. The probe beam was turned on before (dotted line) and after (solid line) reflection from the mirror [5].

netic structures with much smaller periods, preferably on the scale of a micron, are required.

1.3.2.2 Micro-Fabricated Grooved Magnetic Mirrors

The fabrication of an array of magnets of alternating polarity with periods down to 1 μm presents a considerable technical challenge. Model calculations (e.g., Figure 1.10c) show that a grooved perpendicularly magnetized structure (Figure 1.1b) produces a magnetic field distribution the same as that above an array of magnets of alternating polarity (Figure 1.1a), but with the characteristic surface field B_0 reduced by a factor of two [10]. Thus, the grooves behave as missing magnets of opposite polarity to that of the tiny magnets in the protrusions. Grooved magnetic structures may be readily fabricated with micron-scale periods and with excellent surface topology using micro-fabrication techniques such as electron-beam lithography, photolithography, or reactive ion etching.

We have found that by using perpendicularly magnetized films, such as $Co_{80}Cr_{20}$ or $Tb_6Gd_{10}Fe_{80}Co_4$, deposited on a grooved non-magnetic substrate, it is possible to fabricate high-quality magnetic structures with periods down to 1 μm [9, 10, 59]. Magnetic force microscopy (MFM) scans of the magnetic microstructures show that the variation of B_z with y is approximately sinusoidal, even at distances very close ($z \approx 0.05\,\mu m$) to the surface. The sinusoidal shape at small distances is attributed to rounding of the top edges of the groove walls, which reduces the contribution of higher order spatial harmonics (Eq. (1.1)). The magnitude of the B_z component is found to decrease exponentially with distance z, with decay length $a/2\pi$. For grooved microstructures coated with ferromagnetic $Co_{80}Cr_{20}$ film [9, 10], the MFM scans show evidence of domain structure in the regions above the protrusions, with a size $\sim 0.5\,\mu m$, while at distances greater than 0.5 μm the magnetic inhomogeneities have decayed away, consistent with a domain size of about 0.5 μm. Hysteresis loop measurements for the $Co_{80}Cr_{20}$ films exhibit a rhombohedral shape with a coercivity of about 1 kOe and a remanent magnetization of ~25 % of the saturation magnetization (typical of $Co_{80}Cr_{20}$), indicating that not all the domains remain oriented after the magnetizing process. The saturation magnetization for $Co_{80}Cr_{20}$ is $\approx 5\,kG$; so for grooved microstructures with $a = 1\,\mu m$ and $t = 0.2\,\mu m$ the characteristic surface field is estimated to be $B_s \approx 280\,G$.

TOF absorption measurements for laser-cooled atoms dropped from a height $h = 18\,mm$ onto $15 \times 15\,mm^2$ $Co_{80}Cr_{20}$ magnetic microstructures show strong reflection signals similar to Figure 1.2. For Cs $|F = 4, m_F = +4\rangle$ atoms incident on an $a = 1\,\mu m$ microstructure the distance of closest approach is $z_0 \approx 0.3\,\mu m$. Measurements of the spatial distribution of the atom cloud at different times before and after reflection yield a value for the angular spread introduced by the reflection from the grooved mirror of $\Delta\theta_{rms} = (16 \pm 20)$ mrad. To reduce the uncertainties further would require reducing the initial transverse velocity of the atoms, for example, by collimating the atom cloud or by reducing the temperature in the xy plane, or by extending the spatial distribution measurements out to much longer times after the first reflection.

The quality of the grooved magnetic microstructures could be improved, for example, by using *ferrimagnetic* $Tb_6Gd_{10}Fe_{80}Co_4$ films [59] instead of the $Co_{80}Cr_{20}$ film. MFM images taken for $Tb_6Gd_{10}Fe_{80}Co_4$ films show excellent magnetic homogeneity, with no evidence of domain structure. Such films have a magnetization $4\pi M_r \approx 2.8\,\text{kG}$, which for an $a = 1\,\mu\text{m}$, $t = 0.2\,\mu\text{m}$ magnetic microstructure gives a characteristic surface field $B_s \approx 640\,\text{G}$. Our calculations indicate that for the above parameters and using a small bias field to compensate end-effects and stray magnetic fields it should be possible to reduce corrugations so that the angular spread $\Delta\theta_{\text{rms}} < 1\,\text{mrad}$. This type of grooved magnetic microstructure appears to be the most promising approach to date for producing high-quality magnetic mirrors with micron-scale periods.

Although it is possible to fabricate grooved magnetic mirrors with periods smaller than 1 μm the incident atoms will then start to approach so close to the surface that van der Waals forces and the Casimir–Polder force become significant [13], (Chapters 4 and 5).

1.3.2.3 Micro-Fabricated Array of Current-Carrying Conductors

Magnetic mirrors based on periodic arrays of current-carrying conductors have a number of features. Each element in the series array carries the same current and hence produces the same magnetic flux, allowing the production of very flat mirrors, and the ability to control the current allows the magnetic field to be varied, switched, or modulated.

For an infinite array of *narrow* wire conductors alternately carrying equal currents I in opposite directions, the components and the magnitude of the magnetic field above the array are given by expressions similar to Eq. (1.1), but with a characteristic surface field $B_0' = 8\pi I/a$ and a geometrical coefficient of unity instead of '1/3' in the second-order term [11]. For a finite array of wires, the magnetic field distribution above the array may approximate the infinite case by adding two compensating wires each carrying half the normal current to the ends of the array at half the normal spacing [11].

To demonstrate the principle of such a mirror we constructed an $a = 330\,\mu\text{m}$ planar array of 42 parallel gold conductors with two compensating wires on the ends (Figure 1.3) prepared on a silicon wafer by UV photolithography and electroplating techniques [11]. The gold conductors were 60 μm wide, 10 μm thick, and 8 mm long.

TOF absorption signals recorded for $|F = 4, m_F = +4\rangle$ cesium atoms dropped from a height $h = 20\,\text{mm}$ onto the current-carrying wire mirror when activated with 3 A, 12-ms current pulses to coincide with the arrival of the falling atoms indicate a reflectivity close to 100 %. When the duration of the current pulse is reduced to much less than the spread of arrival times of the atoms, the TOF signal sharpens significantly due to 'velocity filtering' in the vertical direction. Studies of the dependence of the reflection signal on current through the wires show a reflection threshold at 0.45 A, followed by three steeply rising regions which are identified as representing the sequential reflection of atoms in the $m_F = +4$ (and $+3$), $+2$ and $+1$ magnetic states.

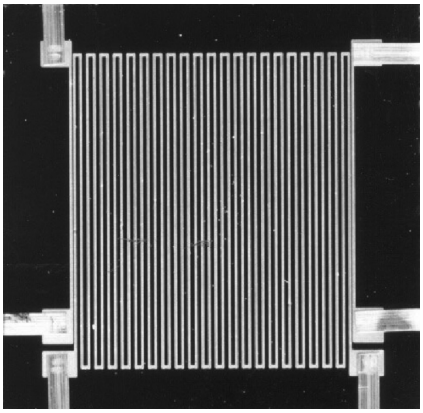

Figure 1.3 Photograph of the current-carrying wire mirror, consisting of a 330-μm-period array of 42 parallel gold wires and two compensating wires on the end [11].

Studies of the spatial distribution of the reflected atoms indicate that at the pulse current of 3 A, which corresponds to a characteristic surface field of $B_0' = 230\,\mathrm{G}$, and without activating the compensating end-wires the reflection is predominantly specular ($\Delta\theta_{\mathrm{rms}} \approx 20\,\mathrm{mrad}$), while at 1 A, corresponding to $B_0' = 77\,\mathrm{G}$, the reflection is much more diffuse ($\Delta\theta_{\mathrm{rms}} \approx 120\,\mathrm{mrad}$) as a result of atoms approaching close to the surface where corrugations due to higher order spatial harmonics become significant.

We estimate that it should be possible to reduce the period of the mirror by at least an order of magnitude, thereby producing a 'harder' mirror and also a flatter mirror by reducing corrugations due to end-effects. Model calculations for an $a = 30$-μm mirror with 10-μm square wires carrying 3 A and with no compensating end-wires indicate a relative corrugation $C \approx 0.003$ for $h = 20\,\mathrm{mm}$, giving $\Delta\theta_{\mathrm{rms}} \approx 4\,\mathrm{mrad}$.

1.3.2.4 Magneto-Optical Recording of Magnetic Microstructures

Certain TbGdFeCo compositions, such as $Tb_{15}Fe_{79}Co_6$, exhibit a relatively low Curie temperature, allowing magnetic structures to be written with a focussed laser beam in the presence of an external magnetic field. Such magneto-optical recording offers the prospect of writing fine and also complex structures.

By mounting a pre-magnetized $Tb_{15}Fe_{79}Co_6$ film on an optical diffraction ruling engine and using a tightly focused diode laser beam in the presence of an external magnetic field oriented in the opposite direction to the film magnetization, magnetic microstructures have been written with linewidths down to about 1 μm and periods down to $a \approx 2\,\mu\mathrm{m}$ [56]. The films are 0.18 μm thick and have a Curie temperature of about 220 °C, a room temperature coercivity of 1.1 kOe, a remanent (perpendicular) magnetization $4\pi M_r \approx 2.4\,\mathrm{kG}$, and an estimated $B_0 \approx 100{-}200\,\mathrm{G}$ (for $a = 2\,\mu\mathrm{m}$). MFM images taken close to the surface of the ruled structure indicate that the magnetization of the ruled lines is quite uniform; however the unruled regions exhibit striped domain patterns due to some break-up of

the pre-magnetized regions during the recording process [56]. At larger distances ($\approx 0.5\ \mu m$) from the surface the magnetic field gradient due to the striped domain patterns is found to have decayed away and the MFM scans become approximately sinusoidal in the y direction, with an exponential fall off with distance z, with decay length $a/2\pi$.

TOF absorption measurements of laser-cooled cesium atoms dropped from a height $h = 25$ mm onto recorded magnetic structures exhibit strong reflection signals, and spatial distribution measurements of the reflected atoms indicate that the reflection is predominantly specular. It should be possible to improve the specularity by further optimization of the magneto-optical recording process and composition of the alloy.

1.4 The Magnetic Film Atom Chip

1.4.1 Background

Advances in photolithography and micro-fabrication techniques have led to the development of miniature surface-based current-carrying elements for the production of BECs and the precise manipulation of ultra-cold atoms, allowing the construction and integration of networks of microtraps, waveguides, and interferometers on the surface of a substrate [13–15, 55]. Miniaturization and scaling down the dimensions of atom traps allow the use of moderate electric currents in order to produce large magnetic field gradients and curvatures and hence a very tight confinement of atomic waves. These microstructures greatly increase elastic collision rates and allow condensates to be produced in just a few seconds of evaporative cooling.

Permanent magnetic materials may also be used to produce magnetic field configurations that can trap, guide, and precisely manipulate neutral atoms [10, 25, 60]. In a ferromagnetic material the magnetic domains generate magnetic fields which are equivalent to the fields produced by effective surface current loops flowing perpendicular to the magnetization vector around the domain edges. In a uniformly magnetized film with perpendicular anisotropy all the domains are aligned in the same direction and within the bulk the currents of neighboring domains cancel. At the same time a net effective current flows around the perimeter of the film with a magnitude given by the product of the magnetization and the film thickness ($I_{\mathrm{eff}} = M_{\mathrm{r}} \times t$). Using established micro-fabrication techniques such as photolithography, vapor deposition, or laser ablation, arbitrary shapes of magnetic film can be fabricated. As examples, a straight edge of a magnet in combination with a uniform external magnetic field will generate a 2D quadrupole potential [10] and a Z-shaped edge of a perpendicularly magnetized film will produce an IP magnetic trap [61]. The use of integrated materials (magnetic films, microwires, and electric

field elements [62]) provides flexibility and extends the capability of integrated atom optics devices.

Various technical limitations can affect applications of current microcircuits on atom chips [13–15]. Large current densities are required to produce large magnetic field gradients and this can lead to excessive heat generation, microwires pealing off, and broken circuits. Current noise from power supplies increases heating rates and limits the condensate lifetime. Johnson thermal noise radiated by a micro-wire conductor leads to spin-flips which affect the BEC lifetime [63]. Permanent magnetic microstructures can replace current microcircuits on atom chips and overcome many of these problems.

Typical permanent magnetic films have a relatively large resistance and a thickness less than 1 μm which suppress radiated thermal magnetic noise. It is expected that permanent magnetic films will produce ultra-stable magnetic potentials and low heating rates. Magnetic films with perpendicular anisotropy, which are used in new-generation hard disk media, provide additional stability of the magnetic field and allow finer magnetic microstructures.

1.4.2
BEC on a Magnetic Film Atom Chip

Permanent magnetic microstructures can produce quadrupole magnetic potentials and with the use of external bias fields can allow adjustment of the position and tightness of the trap. However, the capture volume of the traps is small and the number of cold atoms trapped is not sufficient for efficient evaporative cooling. In order to improve the efficiency of atom capture we combine the permanent magnetic film with current-carrying wires using a two-layer structure (Figure 1.4) [43].

An H-shape plus two end-wire structure was machined in a 0.5-mm-thick silver plate and glued to a ceramic plate to form the bottom layer. The wires have a width of 1 mm and can carry a continuous current of 30 A with an associated temperature rise of no more than 40 °C. The H-shape structure can be arranged for both U and Z-shape currents for quadrupole and IP potentials, respectively.

The top layer of the chip is formed by two 300-μm-thick glass slides ($40\times23\,\mathrm{mm}^2$) glued to the silver structure. High magnetic field gradients require a large effective surface current of the magnetic film and hence large values of the magnetization M_r and/or thickness t. We choose to use ferrimagnetic $Tb_6Gd_{10}Fe_{80}Co_4$ films which exhibit strong perpendicular magnetic anisotropy, an almost square hysteresis loop with a remanent magnetization $4\pi M_r = 2.8\,\mathrm{kG}$, a coercivity $4\pi H_c = 4\,\mathrm{kOe}$, and a Curie temperature $T_C \approx 300\,^\circ\mathrm{C}$. The composition of the alloy is chosen to be a compromise between the desire to have large magnetization, high coercivity, and high Curie temperature. One of the slides is coated with a 0.9-μm-thick $Tb_6Gd_{10}Fe_{80}Co_4$ film (effective current 0.2 A). A long polished edge (Figure 1.4a) together with a bias field generates a quadrupole radial potential. Parallel currents in the two end-wires (separation 9 mm) provide axial confinement and conversion to a 3D IP trap. Both slides are finally coated with a 100-nm-thick gold film.

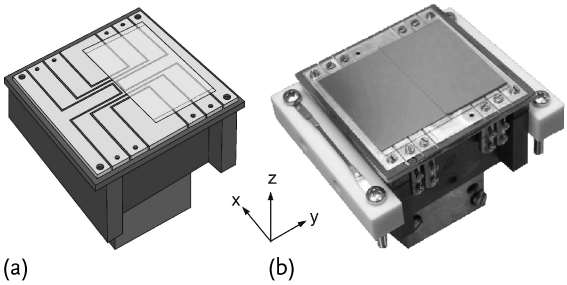

Figure 1.4 Schematic diagram (a) and photo (b) of the magnetic film atom chip [42].

We use a four-beam mirror magneto-optical trap (MMOT) [20] with a quadrupole magnetic field (10 G/cm) provided by two coils located outside the UHV chamber. Two of the laser beams are incident at 45° and are reflected by the gold coating of the chip. They are complemented by two counter-propagating horizontal beams. The volume of the trap is determined by the 35 mm diameter of the laser beams, and the center of the MMOT is located $\sim$ 5 mm below the chip surface. The trapping laser is detuned 18 MHz below the $F = 2 \rightarrow F = 3$ cycling transition in ^{87}Rb and has an intensity of 8 mW/cm^2. The repumping laser is combined with the four trapping beams and tuned to the $F = 1 \rightarrow F = 2$ transition.

The experimental cycle typically lasts 40 s and begins with the application of 6.5 A current through a dispenser (Figure 1.4b) producing ^{87}Rb atoms. About 5×10^8 atoms are collected in the MMOT in 10 s. We turn off the current through the dispenser and allow another 25 s for the UHV vacuum to recover (to typically 2×10^{-11} Torr) before transferring the trapped atoms to the chip-based potentials. The current through the external quadrupole coils is ramped down, the current through the U-wire is ramped up to 8 A and the bias magnetic field raised to 7.3 G. This procedure loads the rubidium atoms into the U-wire MMOT centered at 1.6 mm from the chip. A 2-ms far-detuned (−56 MHz) cooling stage allows the temperature of the atoms to be reduced from 140 to 40 μK. The trapping light and the U-wire current are switched off and a 200-ms σ^+-polarized pulse tuned to the transition $F = 2 \rightarrow F = 2$ optically pumps the atoms into the weak field-seeking state $|F = 2, m_F = 2\rangle$ in the presence of a bias field. A total of 4×10^7 atoms are loaded into the mode-matched IP trap when a current of 21.5 A is applied to the Z-shaped wire and the bias magnetic field is simultaneously increased to 13 G. The magnetic trap is further compressed by ramping the Z-wire current up to 31 A and the bias field up to 40 G. The compressed trap is located 550 μm from the film surface; the radial and axial trap frequencies are 530 and 18 Hz, respectively, and the estimated elastic collision rate is 160/s.

Evaporative cooling to the BEC transition proceeds in two stages. Firstly, RF current is applied to the two end-wires (Figure 1.4a) and its frequency is logarithmically ramped down in 9 s to 1.15 MHz. The number of trapped atoms decreases to 2×10^6 while the temperature is reduced to around 3 μK. The atoms are then loaded into the magnetic film trap by removing the current in the Z-wire and increasing the bias field to 47 G. Radial confinement of the trap is provided by the edge of

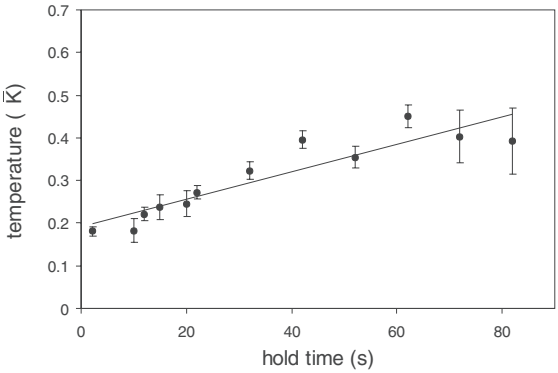

Figure 1.5 Measurements of the heating rate in a magnetic film microtrap located 210 μm from the surface [64].

the permanent magnetic field of the film and axial confinement is provided by two end-currents generated by an ultra-stable power supply. The frequency of a second RF field is ramped for 2 s from 1.5 down to 0.73 MHz. At the end of the evaporative cooling a BEC of typically 10^5 atoms is formed 100 μm from the surface. In order to minimize the effect of the permanent magnetic field from the film in a TOF expansion of the cloud we move the atoms to 1 mm from the film before releasing them.

The heating rate of an ultra-cold atomic cloud captured in the magnetic film trap 210 μm from the film (radial frequency 120 Hz) was measured by TOF temperature measurements after various hold times (Figure 1.5). The observed heating rate of 3.2 nK/s [64] is remarkably low, and is to be compared with the heating rate of atoms in the Z-wire trap of 270 nK/s. The low heating rate is a promising feature of the magnetic film atom chip.

1.4.3
Spatially Resolved RF Spectroscopy to Probe Magnetic Film Topology

Studies with atom chips based on current-carrying conductors have revealed that ultra-cold atomic clouds can exhibit fragmentation along the axial direction, which is related to the roughness of the wire surface and edges and to internal granular structure of the conductor [65]. This roughness leads to small deviations in the current path and correspondingly to a spatially varying axial magnetic field component which corrugates the trapping potential.

We have studied quantitatively the fragmentation of ultra-cold ^{87}Rb atoms on the magnetic film atom chip using a combination of spatially resolved imaging and RF spectroscopy of the atoms [66]. An atomic cloud was evaporatively cooled in the Z-wire IP trap down to 5 μK, loaded into the magnetic film trap at four different distances $z_0 = 57$, 67, 87, and 115 μm from the film and allowed to expand axially 5 mm by decreasing the end-currents to 0.5 A. The narrow energy distribution of the ultra-cold trapped atoms is greatly affected by small variations of the trapping

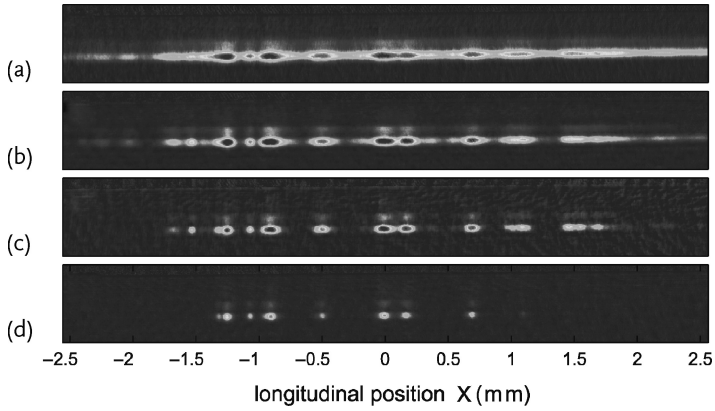

Figure 1.6 Absorption images of the atomic density in the elongated magnetic film trap located 67 μm below the film at different values of the cut-off frequency ν_f: (a) 1238 kHz, (b) 890 kHz, (c) 766 kHz, (d) 695 kHz [66].

potential, and the spatial distribution of the atoms reveals small corrugations in the potential [67]. A RF field is applied in a direction perpendicular to the quantization magnetic field and its frequency is swept from 2 MHz down to a cut-off frequency ν_f ranging from 1.4 to 0.5 MHz. The atoms in the high energy tail of the distribution are resonant with the RF field and are outcoupled to untrapped states leaving a truncated Boltzmann distribution. The bias field is turned off after the sweep, allowing the atoms to accelerate away from the film. The longitudinal distribution is unperturbed during the 1 ms expansion and is optically imaged with a spatial resolution of 5 μm. Variations in the axial extension of the cloud become noticeable when ν_f is reduced below 1.3 MHz (Figure 1.6a). Reducing the cut-off frequency further results in well-separated clumps of atoms which accumulate in the lowest potential wells (Figure 1.6d).

For a quantitative analysis of the experimental data we use an expression for the atomic density of a truncated Boltzmann distribution [66, 68] integrated over coordinates y and z

$$n(x,\beta) = n_0(x)\left[\mathrm{erf}\left(\sqrt{\beta}\right) - 2\sqrt{\beta/\pi}\mathrm{e}^{-\beta}(1+2\beta/3)\right], \tag{1.4}$$

where the truncation parameter β is a function of the coordinate x, the cut-off frequency ν_f, the temperature T, and the value of the magnetic field $|B_x(x) + B_0|$ at the bottom of the trap:

$$\beta(x,\nu_f) = \left[m_F h\nu_f - m_F g_F \mu_B\,|B_x(x) + B_0|\right]/k_B T\,. \tag{1.5}$$

For each distance z_0 from the film a set of RF spectroscopy measurements is taken and the local value of the magnetic field at the coordinate x is extracted. The rms amplitude increases with distance z_0 (measured in μm) according to the approximate power-law (Figure 1.7)

$$B_{x,\mathrm{rms}} = 1.32\times 10^4 \times z_0^{-1.85} \quad [\mu\mathrm{T}]\,. \tag{1.6}$$

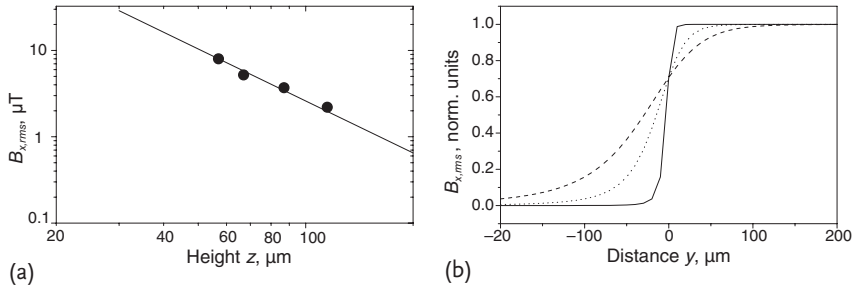

Figure 1.7 (a) Dependence of the magnetic-field roughness $B_{x,\mathrm{rms}}$ on height z. The solid line was obtained using Eq. (1.5). (b) Dependence of the normalized field roughness predicted by the model (Eq. (1.7)) on the transverse coordinate y for heights 10 μm (solid), 50 μm (dotted), and 100 μm (dashed line) [66].

Stylus profilometer measurements indicate that the rms roughness of the polished edge of the slide is around 10 nm over a 400-μm scale. The associated deviations of the effective current path cannot explain (i) the large rms values of the corrugated axial magnetic field and (ii) the observed $z_0^{-1.85}$ dependence. When the cloud is positioned $z_0 = 50$ μm below the magnetic surface substantial fragmentation is observed. However, when it is positioned 50 μm below the non-magnetic gold surface the density distribution exhibits a rather smooth profile. These observations indicate that the random component of the magnetic field originates from the bulk of the magnetic film as a result of inhomogeneous magnetization and not from variations of the film edge.

We have developed a model [66] to study how the variations in the film magnetization generate a random magnetic field. For white-noise fluctuations in the magnetization the rms amplitude of the magnetic noise is

$$B_{x,\mathrm{rms}} = \sqrt{\frac{3}{\pi}}\frac{\mu_0 t d_0 \Delta M}{16 z^2}\sqrt{1+\frac{15}{8}\alpha-\frac{5}{4}\alpha^3+\frac{3}{8}\alpha^5}\,, \tag{1.7}$$

where $\alpha = y/\sqrt{y^2+z^2}$, t is the film thickness, d_0 is the characteristic feature size of the domains, and ΔM is the rms value of the magnetization variations. Below the edge of the film ($y = 0$) the model predicts that the random magnetic field decays with a z_0^{-2} dependence which is consistent with the observed $z_0^{-1.85\pm0.3}$ dependence. This is slower than the $z_0^{-2.5}$ decay of a corrugated field below current-carrying microwires [69, 70]. The model predicts an even faster decay of the random component for $y < 0$ (Figure 1.7b). Using the experimental rms values and a characteristic domain size $d_0 \approx 5$ μm we estimate the level of inhomogeneity $\Delta M/M_\mathrm{s} \simeq 0.3$, where M_s is the saturation magnetization of the TbGdFeCo film. If we assume the inhomogeneity originates from reversal of a small number of domains and assume a binomial distribution of the reversal then the mean magnetization is about $0.9M_\mathrm{s}$.

The observed magnetic inhomogeneity in the TbGdFeCo films is attributed to some deterioration during vacuum bake-out (140 °C for 4 days) of the magnetic

film atom chip. It was found that such deterioration can be avoided by maintaining the temperature below 100 °C.

1.4.4
Adiabatic Splitting of a BEC for Asymmetric Potential Sensing

The idea of using adiabatic splitting of a BEC for sensing asymmetric potentials is based on the assumption that during an adiabatic splitting process the fractional number of atoms in each well of a double-well potential is proportional to the potential difference between the bottoms of the wells as long as the chemical potential is larger than the barrier height [71]. The situation is similar to two coupled pools of superfluids which have the same level of fluid and the deeper pool will contain more fluid than the shallower pool.

Studies of the magnetic field topology in Section 1.4.3 revealed a double-well structure near the center of the film ($x \sim 0$, Figure 1.6c,d) with very similar characteristics for both wells. One of the features of the random nature of the corrugated magnetic field is that the Fourier components decay exponentially with height and the short-wavelength components decay much faster than the long-wavelength components. As a result the barrier between the two wells decreases substantially when the atomic cloud is moved away from the film and the double-well structure merges into a single well.

Using various values of the bias field an ultra-cold cloud is positioned at different heights, and the 1D spatial distribution of the atoms is probed by optical imaging. The cloud temperature is measured by TOF expansion. The spatial dependence of the trapping potential is determined from the Boltzmann distribution law $V(x) = -k_B T \ln(n(x))$ and the double-well parameters (separation and barrier height) are extracted by fitting the measured potential to a model potential [64]. For a bias field of 2.6 G the coalescence point is located 175 μm from the film. Increased values of the bias field move the trap closer to the surface and split it into a double well in the longitudinal (x) direction. The measurements show that the barrier height can be adjusted from sub-kHz up to 100 kHz and the well separation can be up to 180 μm.

Accurate knowledge of the double-well potential was used for precise control of the splitting of the BEC. The splitting process and the associated distribution of atoms between the two wells are extremely sensitive to the presence of any asymmetry component Δ between the bottoms of the two wells [71]. In such a case the number of atoms in the deeper well is greater than in the shallower well and is determined by the trap frequencies of both wells (by sheer accident these parameters defined by the corrugated potential are almost identical) as well as external magnetic fields or gravity gradients. An asymmetric potential can be either compensated or intentionally introduced by applying a current imbalance between the end-wires on the chip (Figure 1.4a). A calibration of the applied potential asymmetry was carried out using RF spectroscopy [71]. Two BECs separated by 170 μm are initially produced in a symmetric double-well potential with a barrier height of several kHz. A large current imbalance of 1 A is introduced in the end-wires for a duration of 500 ms, thereby tilting the wells. A 1-ms RF pulse of variable frequency

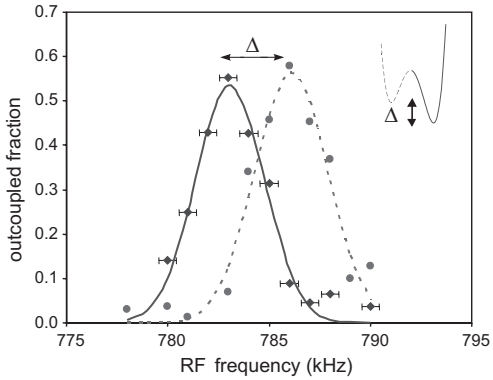

Figure 1.8 Outcoupling of atoms from two condensates in an asymmetric double well as a function of RF frequency [71].

ν_f is applied to resonantly outcouple those atoms from either well that are resonant with the RF field ($h\nu_f = \mu_B g_F B$). Optical imaging of the remaining atoms provides a measure of the number of outcoupled atoms as a function of ν_F (Figure 1.8). The resulting spectra yield an applied magnetic potential gradient of 32 Hz/μm for the current imbalance of 1 A.

A small condensate of 46 000 atoms is produced in a single well 175 μm from the film. A calibrated asymmetric potential is then applied via a current imbalance in the end-wires that is variable between ±120 mA. The bias magnetic field is slowly increased (over 2 s) between 2.5 and 2.7 G, splitting the condensate axially by 70 μm in the double well located 155 μm from the film. At this position the barrier height is about 25 % of the chemical potential. At the end of the adiabatic splitting the bias field is quickly increased (over 10 ms) to ramp the barrier above the chemical potential and to preserve the fractional distribution of the atoms. Absorption imaging determines the fractional number of atoms for various values of the applied calibrated asymmetry (Figure 1.9). The shot-to-shot noise level of 2.8 % pro-

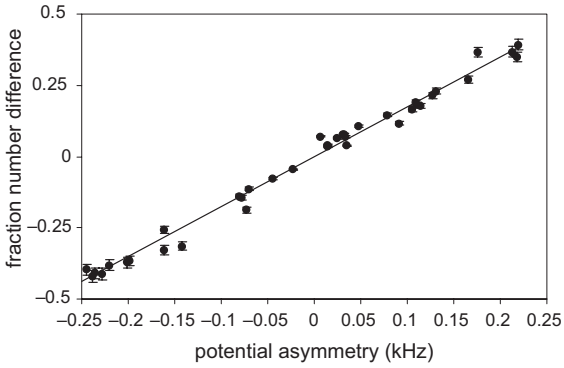

Figure 1.9 Measurements of the fractional number difference (circles) in the two wells as a function of the applied potential asymmetry. Solid line represents a linear fit [71].

vides a single-shot sensitivity of 17 Hz for the potential well energy imbalance for a 70 μm separation. This method of measuring the fractional distribution of atoms is suitable for the construction of sensors of gravitational field gradients. The demonstrated single-shot sensitivity to analogous changes in gravity is $\delta g/g = 2 \times 10^{-4}$ for a 70 μm separation [71] which corresponds to an 8-nm height difference between the two wells. At present the demonstrated sensitivity to potential gradients is well below the sensitivity of free-space atom interferometers [72] but surpasses the sensitivity of on-chip BEC interferometers which are currently limited by relatively short decoherence times.

1.4.5
Spatially Inhomogeneous Phase Evolution of a Two-Component BEC

Accurate knowledge of the phase of matter waves is an important factor in studying BEC coherence, and in potential future applications of BEC interferometers. We have studied the relative phase evolution of an elongated two-component BEC composed of the $|F = 1, m_F = -1\rangle$ and $|F = 2, m_F = 1\rangle$ hyperfine ground states of ^{87}Rb atoms [73], magnetically trapped on an atom chip [43]. These two states are particularly attractive for trapped-atom interferometry because the first-order Zeeman shift between them is canceled at a magnetic field of 3.23 G. To improve the relative phase detection we developed an imaging technique to simultaneously measure the column density of each hyperfine state during TOF expansion [73]. Our dual-state detection produces sub-percent uncertainty in the measured relative population while preserving the spatial mode of each state.

We prepare a condensate in a superposition of the two hyperfine states and interrogate the relative phase evolution using two-photon microwave-radiofrequency Ramsey interferometry. The inter- and intra-state scattering lengths have slightly different values and, as a result, the prepared superposition is in a non-equilibrium state [74], leading to undamped collective oscillations and complex spatial modes of each component. We focus [73] on the dynamics of the relative phase along the direction of weak (axial) confinement. The relative phase begins (after the first $\pi/2$ pulse) spatially uniform, then becomes inhomogeneous along the axial coordinate, varying by 1.9π across the condensate after 90 ms of evolution.

The second $\pi/2$ pulse converts spatial variations of the relative phase into spatial variations of the atomic density of each state. The time dependence of the relative phase is accompanied by interference in space and, as a result, spatial fringes appear in the absorption images (Figure 1.10) and change with the evolution time. The spatial dependence of the relative phase leads to inhomogeneous dephasing of the condensate wavefunction along the axial direction, and we observe a relatively fast decay of the Ramsey interference fringes (decay time ∼70 ms). We emphasize that, under our conditions, inhomogeneity of the relative phase of the condensate wavefunction is the dominant mechanism for the loss of the Ramsey fringes, rather than decoherence due to coupling to the environment or quantum phase diffusion.

Our observations of the spatial evolution of the relative phase and the inhomogeneous dephasing of the condensate wavefunction are well described by a mean-

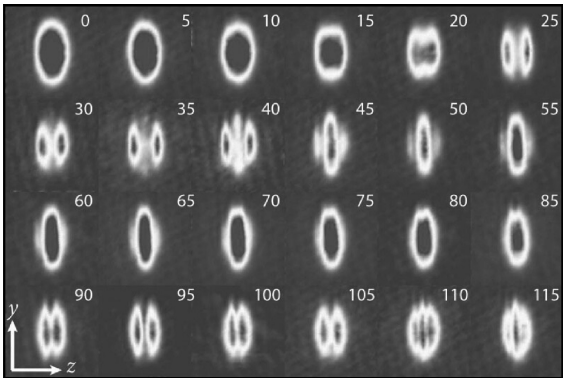

Figure 1.10 Single shot absorption images of the condensate in the state $|F = 2, m_F = +1\rangle$ taken after 20 ms of free fall and expansion with varying Ramsey interferometry time (in ms). Application of the second $\pi/2$ pulse locally converts the relative phase into atom number density and leads to the appearance of spatial fringes along the z (axial) coordinate [73].

field formalism and supported by numerical solutions [73] of the coupled Gross–Pitaevskii equations for both components with decay terms corresponding to inter- and intra-state many-body loss mechanisms.

1.4.6
BEC on Other Permanent-Magnet Atom Chips

A number of permanent-magnet atom chips constructed from different types of magnetic media have been used for the production of BECs. The group at Imperial College, London [41] have used 3.5-μm-thick videotape with a sinusoidal pattern of in-plane magnetization. The pattern has a period of 106 μm and provides a surface magnetic field of 110 G, and in combination with a bias field of 1 G forms an array of waveguides 80 μm from the surface. ^{87}Rb atoms are initially trapped in the MMOT, loaded into an H-shape IP magnetic trap, further cooled via RF evaporation, and then loaded into the videotape microtrap with trap frequencies of 450 Hz (radial) and 15 Hz (axial) at a temperature of 10 μK. Further evaporative cooling in the permanent-magnet microtrap produces a condensate with about 8×10^4 rubidium atoms which is detected via anisotropic TOF expansion in free-flight or in the appearance of a bimodal distribution in a 1D waveguide expansion. Studies of axial center-of-mass motion and a breathing mode revealed decaying oscillations with a damping time of 180 ms which was associated with a slight roughness in the magnetic potential. The material of the videotape exhibits insulating properties and should lead to a strong suppression of spin-flips due to thermal Johnson noise. Measurements of the thermal cloud lifetime demonstrated long lifetimes ranging from 15 to 35 s at distances of 15 and 40 μm below the surface.

The group at MIT [44] have used a prototype hard-disk medium consisting of a 23-nm-thick Co-Cr-Pt-based oxide layer with perpendicular anisotropy and a 200-

nm-thick magnetically soft underlayer with a total magnetization of 470 emu/cm^3. A pattern with alternating magnetization of period 100 μm was written on the magnetic substrate. Ultra-cold atoms were loaded into a single microtrap in which axial confinement was accomplished by a Z-shape wire located below the disk. RF evaporation led to the production of 50 000 condensed atoms in the permanent magnetic microtrap with trap frequencies of 390 Hz (radial) and 9 Hz (axial). Optical imaging revealed a bi-modal distribution with a condensate fraction >80 %. A lifetime of ~30 s was reported for a height 40 μm above the surface. Tight radial confinement with a frequency of 16 kHz was demonstrated with a smaller period (10 μm) of the written structure. During 1D expansion of the BEC in a waveguide a break-up of the atomic cloud was detected at distances closer than 40 μm. This break-up is associated with perturbations of the axial magnetic confinement due to variations in the magnetic moments of domains and edge-effects during writing of the periodic magnetic structure.

The group in Amsterdam [45] have constructed a permanent-magnet atom chip consisting of in-plane magnetized 40-μm-thick Fe-Pt foil with a machined F-shaped self-biased IP trap with frequencies of 11 kHz (axial) and 30 Hz (radial) at 180 μm from the surface. The permanent magnetic trap was loaded by transporting atoms from a quadrupole magnetic trap by a combination of external magnetic fields. RF spectroscopy was employed to analyze the cloud temperature and the atomic distribution in the trap and to observe the onset of Bose condensation *in situ* without expansion from the trap.

1.5
Permanent Magnetic Lattice on a Magnetic Film Atom Chip

1.5.1
Background

Optical lattices have been used extensively to manipulate and control periodic arrays of ultra-cold atoms and quantum degenerate gases [75], for example, in studies of low-dimensional quantum gases [76, 77], quantum tunneling experiments such as the superfluid to Mott insulator quantum phase transition [78] and experiments on BECs in disordered potentials such as Anderson localization [79, 80]. Optical lattices also have potential application in quantum information processing since they can provide storage registers for qubits based on neutral atoms [81, 82].

An alternative approach for producing periodic lattices for ultra-cold atoms is based on periodic arrays of permanent magnetic microstructures on a magnetic film atom chip [49, 83, 84] using the magnetic micro-structure technology developed for magnetic mirrors [9, 10]. Simple 1D magnetic lattice structures consisting of arrays of 2D traps have been proposed [55, 83] and constructed using current-carrying conductors [85] and video tape [86], though loading of atoms into multiple lattice sites was not demonstrated. 2D lattices of magnetic microtraps with non-zero potential minima have been proposed based on crossed arrays of current-

carrying conductors plus bias fields [87, 88] and on crossed arrays of perpendicularly magnetized grooved films plus bias fields [83]. Other geometries for constructing 2D magnetic lattices have also been proposed, including a single layer of periodic arrays of square-shaped magnets with three different thicknesses [83, 84] and periodic arrays of patterned asymmetric Z-shaped structures [46].

Permanent magnetic lattices have some distinctive characteristics. They have highly stable, reproducible potentials, low technical noise, and extremely low heating rates. They can have large barrier heights and large trap curvature, leading to high trap frequencies. They can be constructed with a wide range of periods, down to about 1 μm, and can have tailored complex potentials. They can be readily scaled to have a large number of lattice sites, for example, a 1-μm-period $10 \times 10\,\mathrm{mm}^2$ 2D lattice has 10^8 sites, which could be very useful as a storage register for quantum information processing. They are static and not dynamic; however they can be used in conjunction with current-carrying wire traps to load atoms into the lattice. The atoms need to be prepared in low-field seeking states in order to be trapped, allowing RF evaporative cooling *in situ* and the use of RF spectroscopy. Finally, permanent magnetic lattices are suitable for integration onto an atom chip and for devices. Thus, magnetic lattices may be considered to be complementary to optical lattices, in much the same way as magnetic traps and optical dipole traps are complementary.

1.5.2 Basic Principles

1.5.2.1 One-Dimensional Magnetic Lattice

We first consider the simple case of a 1D magnetic lattice, similar to the periodic grooved magnetic mirror described in Section 1.3 but with the addition of bias fields B_{1x} and B_{1y} (Figure 1.11). For an infinite 1D magnetic array with period a, film thickness t and perpendicular magnetization, the components of the magnetic field for distances $z \gg a/4\pi$ above the array are given by [83]

$$\left[B_x; B_y; B_z\right] = \left[B_{1x}; B_{0y}\mathrm{e}^{-kz}\sin ky + B_{1y}; B_{0y}\mathrm{e}^{-kz}\cos ky\right], \tag{1.8}$$

where $k = 2\pi/a$, $B_{0y} = B_0(1 - \mathrm{e}^{-kt})\mathrm{e}^{kt}$ and $B_0 = 4M_z$ (Gaussian units).

The potential minimum (trap bottom), trap height, barrier heights, and trap frequencies (for a harmonic potential) are given, respectively, by [83]

$$\begin{aligned} &B_{\min} = |B_{1x}|, \quad z_{\min} = \frac{a}{2\pi}\ln\left(\frac{B_{0y}}{B_{1y}}\right), \quad \Delta B^y = \left(B_{1x}^2 + 4B_{1y}^2\right)^{1/2} - |B_{1x}|, \\ &\Delta B^z = \left(B_{1x}^2 + B_{1y}^2\right)^{1/2} - |B_{1x}|, \quad \omega_y = \omega_z = \frac{2\pi}{a}\left(\frac{m_{\mathrm{F}} g_{\mathrm{F}} \mu_{\mathrm{B}}}{M|B_{1x}|}\right)^{1/2} |B_{1y}|. \end{aligned} \tag{1.9}$$

All of these quantities may be controlled by the bias fields B_{1x} and B_{1y}.

Figure 1.11c–e shows numerically calculated contour plots of the magnetic fields for a finite 1D magnetic lattice and the parameters given in the caption. With no

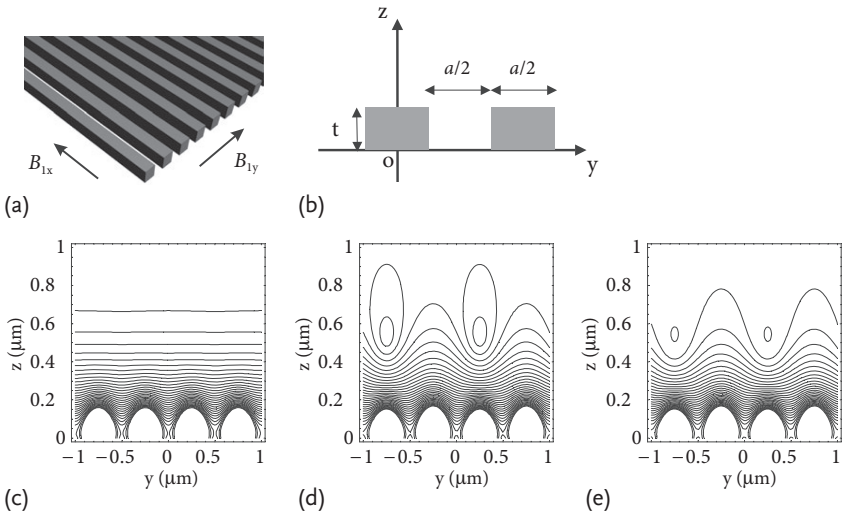

Figure 1.11 (a, b) 1D periodic array of parallel magnets with perpendicular magnetization. (c–e) Numerically calculated contour plots of the magnetic field in the central region in the $y0z$ plane with (c) no bias fields, (d) $B_{1y} = -15\,\mathrm{G}$, and (e) $B_{1x} = -20\,\mathrm{G}$, $B_{1y} = -15\,\mathrm{G}$. 1001 magnets, $a = 1\,\mu\mathrm{m}$, $t = 0.05\,\mu\mathrm{m}$, $l_x = 1000.5\,\mu\mathrm{m}$, and $4\pi M_z = 3.8\,\mathrm{kG}$ [83].

bias fields (Figure 1.11c), the magnitude of the magnetic field falls off exponentially with distance z, representing the simple case of a magnetic mirror [9, 10] as described in Section 1.3.1. With the addition of $B_{1y} = -15\,\mathrm{G}$ (Figure 1.11d), the magnetic field develops 2D magnetic traps with zero potential minima; this configuration can give rise to spin-flips and is not suitable as a lattice for trapping atoms. With the addition of $B_{1x} = -20\,\mathrm{G}$ and $B_{1y} = -15\,\mathrm{G}$ (Figure 1.11e), the magnetic field has 2D magnetic traps with non-zero potential minima, where the trap bottom is given by $|B_{1x}|$.

1.5.2.2 Two-Dimensional Magnetic Lattice

We now consider a 2D magnetic lattice produced by two crossed periodic arrays of parallel magnets, thicknesses t_1 and t_2, separated by a small distance s ($< a/2\pi$), and with bias fields B_{1x}, B_{1y} (Figure 1.12a) [83]. For an infinite *symmetrical* 2D magnetic lattice, the trap minimum, trap height, barrier heights, and trap frequencies (for a harmonic potential) are given, respectively, by

$$B_{\min} = c_1 |B_{1x}| \,, \quad z_{\min} = \frac{a}{2\pi} \ln\left(\frac{c_2 B_{0x}}{B_{1x}}\right) \,, \quad \Delta B^x = \Delta B^y = c_4 |B_{1x}| \,,$$
$$\Delta B^z = c_5 |B_{1x}| \,, \quad \omega_x = \omega_y = \frac{\omega_z}{\sqrt{2}} = \frac{2\pi}{a}\left(\frac{m_F g_F \mu_B c_3}{M|B_{1x}|}\right)^{1/2} |B_{1x}| \,, \tag{1.10}$$

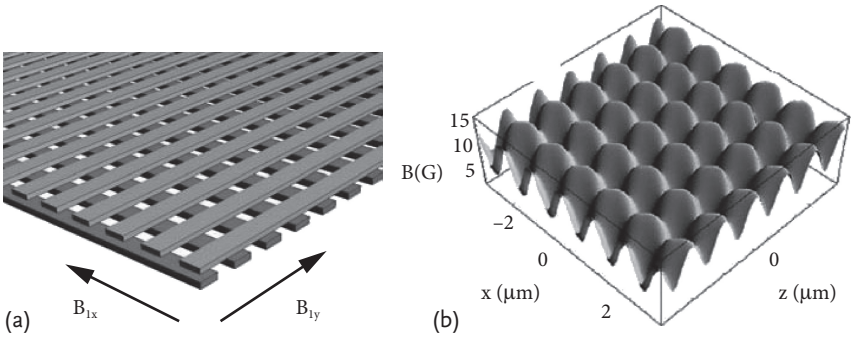

Figure 1.12 (a) 2D periodic array consisting of two crossed layers of parallel magnets with perpendicular magnetization. (b) 3D plot of the magnetic field. 2 × 1001 magnets, $a = 1\,\mu\text{m}$, $t_1 = 0.322\,\mu\text{m}$, $t_2 = 0.083\,\mu\text{m}$, $l_x = l_y = 1000.5\,\mu\text{m}$, $4\pi M_z = 3.8\,\text{kG}$, $B_{1x} = -4.08\,\text{G}$, $B_{1y} = -6.05\,\text{G}$, $B_{1z} = -0.69\,\text{G}$, $\nu_x = \nu_y = 232\,\text{kHz}$, $\nu_z = 329\,\text{kHz}$ [83].

with the constraint $B_{1y} = c_0 B_{1x}$ for a symmetrical lattice. In Eq. (1.10), $B_{0x} = B_0(1 - e^{-kt_2})e^{k(s+t_1+t_2)}$ and the c_i's are dimensionless constants involving only the geometrical parameters a, s, t_1 and t_2 of the magnetic arrays, given in [83]. All of the quantities in Eq. (1.10) may be controlled by the bias field B_{1x}. Figure 1.12b shows the numerically calculated magnetic field for a finite 2D magnetic lattice and the parameters given in the caption.

1.5.2.3 **Permanent 1D Magnet Lattice for Ultra-Cold Atoms**

We have constructed a 1D magnetic lattice with period $a = 10\,\mu\text{m}$ and dimensions $10 \times 10\,\text{mm}^2$ of perpendicularly magnetized $Tb_6Gd_{10}Fe_{80}Co_4$ magneto-optical film deposited on a grooved silicon wafer which was microfabricated by reactive ion etching [49]. The magnetic microstructure is coated with a reflecting gold film for use in a MMOT and mounted on an atom chip, similar to that described in Section 1.4. Beneath the atom chip is a silver plate which was machined to provide a U-wire for a quadrupole trap and 5-mm-long and 30-mm-long Z-wires for IP traps, which are required for loading the permanent magnetic lattice. The atom chip is mounted in the UHV chamber with the permanent magnetic microstructure facing down.

About 10^8 ^{87}Rb atoms are cooled and trapped in the MMOT and transferred to a compressed MOT produced by the U-current plus a bias field $B_{1x} = 7\,\text{G}$. The atoms are further cooled through polarization gradient cooling and optically pumped to the $|F = 2, m_F = +2\rangle$ low-field seeking state. The 5 mm-long Z-wire trap is then turned on, the wire current slowly ramped up to 35 A, and the bias field is simultaneously ramped up to $B_{1x} = 40\,\text{G}$. In this way about 5×10^7 atoms at a temperature of about 200 μK are transferred to the Z-wire trap. After waiting for the trapped atoms to thermalize, the atoms are RF evaporatively cooled to about 0.4 μK to create a BEC in the Z-wire trap about 250 μm below the chip surface where the magnetic field from the permanent magnetic microstructure is negligible. The y-bias field is then ramped up to $B_{1y} = 30\,\text{G}$ with $B_{1x} = 15\,\text{G}$ (trap bottom) to create a 1D magnetic lattice of 2D traps which overlaps the atom cloud. The barrier height

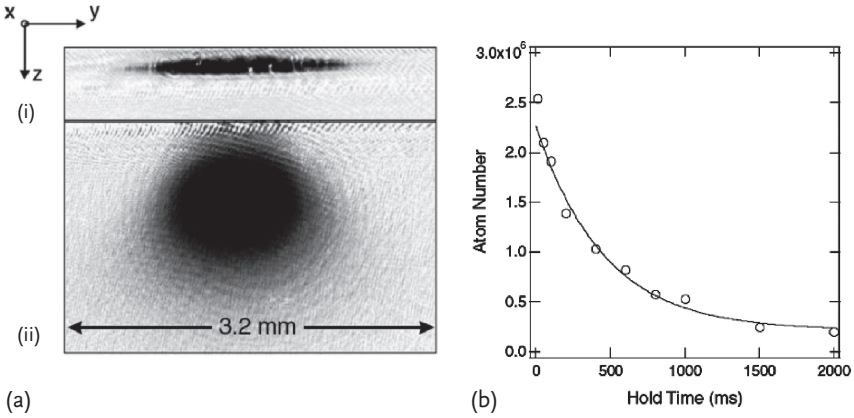

Figure 1.13 (a) Absorption image of atoms released from the magnetic lattice after (i) 4 ms and (ii) 16 ms time of flight. The broken structure in (i) is due to non-uniform reflection of the imaging beam from the grooved structure; (b) Number of atoms remaining in the magnetic lattice as a function of hold time. The solid line represents an exponential fit to the data points with a decay time of 0.45 s [49].

is typically 1.2 mK. About 45 % of the atoms are then transferred adiabatically from the Z-wire trap into the magnetic lattice.

After loading about 5×10^5 ^{87}Rb atoms at 15 μK from the 5-mm-long Z wire trap into the $10 \times 10\,\text{mm}^2$ magnetic lattice, absorption images taken after 14 ms TOF indicate that atoms are trapped in about 150 of the 1000 lattice sites at an estimated 4 μm from the chip surface (Figure 1.13a). It should be possible to trap in most of the 1000 lattice sites by loading from the 30-mm-long Z wire trap. By releasing the atoms from the magnetic lattice (by switching off B_{1y}), the lifetime of the trapped atoms is found to be 0.45 s (Figure 1.13b). With our current pixel image resolution of 9 μm it is not possible to resolve atoms in the individual lattice sites of the $a = 10$ μm magnetic lattice.

Using parametric heating, the radial trap frequencies were found to range up to $\nu_{\text{rad}} = 90\,\text{kHz}$. A small amount of axial confinement, $\nu_{\text{axial}} \approx 1\,\text{Hz}$, is provided by the magnetic field from the surrounding magnetic film. The temperature of the trapped atoms in the magnetic lattice was determined by RF spectroscopy to be greater than 150 μK, which is much higher than the temperature, ∼6 μK, determined from TOF expansion, due to adiabatic compression in the tightly confining magnetic microtraps. We note that the magnetic lattice microtraps are currently highly elongated ($\nu_{\text{rad}}/\nu_{\text{axial}} \approx 5 \times 10^4$), so that the trapped clouds resemble a 1D Bose gas, in which thermalization and hence evaporative cooling is extremely inefficient [77]. In a recent series of experiments [89], we have implemented controllable axial confinement by means of a Z-wire current and have optically pumped the $F = 2$, $m_{\text{F}} = +2$ atoms into the $F = 1$, $m_{\text{F}} = -1$ weak-field seeking state in order to reduce three-body recombination losses. With an aspect ratio $\nu_{\text{rad}}/\nu_{\text{axial}} \approx 40$, we have been able to load $\approx 5 \times 10^5$ atoms into 10 μm-period magnetic lattice and, after evaporative cooling, to reach temperatures of about 2 μK

with a trap lifetime of ~ 10 s. This should allow us to reach quantum degeneracy in the individual magnetic lattice sites and to generate multiply arrays of condensates.

In order to perform quantum tunneling experiments in the magnetic lattice it will be necessary to reduce the lattice period down to $a \approx 2$–4 μm.

1.5.2.4 Other Permanent Magnetic Lattices

The group in Amsterdam [47] have recently realized a 2D array of microtraps above multiple Z-shaped patterns microfabricated in a 300-nm-thick Fe-Pt film ($M_r = 670$ kA/m). The magnetic lattice of ultra-cold ^{87}Rb $F = 2$, $m_F = 1$ atoms (periods 22 μm and 36 μm in orthogonal directions) was produced 10 μm above the surface with very tight confinement (radial and axial frequency 13.4 kHz). Atoms from a macroscopic Z-wire trap were loaded into more than 500 traps and individual traps were optically resolved. Three-body recombination losses were used to characterize the number and temperature of the atoms in the individual traps and show the onset of BEC in 70 sites. However, the average condensate fraction is less than 0.1 which is attributed to the very tight confinement. Transport of the atoms over several lattice sites in one direction and back was demonstrated. A focused laser beam was used to empty one site and move it over several periods. These studies are promising for building a scalable quantum information processor based on neutral-atom permanent-magnet chips.

1.6 Summary and Conclusions

After almost two decades since the initial ideas of surface-based magnetic optical elements for ultra-cold atoms were proposed, the use of atom chips for producing and manipulating clouds of ultra-cold atoms and quantum degenerate gases on a substrate has evolved into a very active new area of research. Atom chips allow the construction and integration of miniature networks of magnetic microtraps, waveguides, and interferometers into a single device. The combination of permanent magnetic materials with dynamic current-carrying conductors to produce complex magnetic field configurations offers a promising way of constructing stable low-noise atom chips with micron-scale elements. Such devices have a wealth of potential future applications as trapped-atom interferometers, sensors of potential gradients, chip-based atomic clocks, microsensors of magnetic field topology and storage registers for quantum information processing.

Acknowledgments

The authors thank the many colleagues who have contributed to the work reported in this article, including Alexander Akulshin, Russell Anderson, Tim Davis, Saeed Ghanbari, David Gough, Brenton Hall, Smitha Jose, Tien Kieu, Leszek Krzemien,

David Lau, Russell McLean, Geoffrey Opat, Timothy Roach, Wayne Rowlands, Falk Scharnberg, Mandip Singh, Chris Ticknor, Michael Volk, James Wang, and Shannon Whitlock. The work is supported by the Australian Research Council.

References

1 Opat, G.I. (1983) In *Proc. 3rd Marcel Grossmann Meeting of General Relativity*, Part B (ed. Hu Ning), Beijing, Science press, Amsterdam, North Holland, p 1491.
2 Wark, S. and Opat, G.I. (1992) *J. Phys. B* **25**, 4229.
3 Opat, G.I., Wark, S.J., and Cimmino, A. (1992) *Appl. Phys. B* **54**, 396.
4 Roach, T.M., Abele, H., Boshier, M.G., Grossman, H.L., Zetie, K.P., and Hinds, E.A. (1995) *Phys. Rev. Lett.* **75**, 629.
5 Sidorov, A.I., McLean, R.J., Rowlands, W.J., Lau, D.C., Murphy, J.E., Walkiewicz, M., Opat, G.I., and Hannaford, P. (1996) *Quant. Semiclass. Opt.* **8**, 713.
6 Hughes, I.G., Barton, P.A., Roach, T.M., Boshier, M.G., and Hinds, E.A. (1997) *J. Phys. B* **30**, 647.
7 Saba, C.V., Barton, P.A., Boshier, M.G., Hughes, I.G., Rosenbusch, P., Sauer, B.E., and Hinds, E.A. (1999) *Phys. Rev. Lett.* **82**, 468.
8 Sidorov, A.I., Lau, D.C., Opat, G.I., McLean, R.J., Rowlands, W.J., and Hannaford, P. (1998) *Laser Physics* **8**, 642.
9 Sidorov, A.I., McLean, R.J., Sexton, B.A., Gough, D.S., Davis, T.J., Akulshin, A., Opat, G.I., and Hannaford, P. (2001) *Compt. Rendus* **2**(4), 565.
10 Sidorov, A.I., McLean, R.J., Scharnberg, F., Gough, D.S., Davis, T.J., Sexton, B.J., Opat, G.I., and Hannaford, P. (2002) *Acta Phys. Polon. B* **33**, 2137.
11 Lau, D.C., Sidorov, A.I., Opat, G.I., McLean, R.J., Rowlands, W.J., and Hannaford, P. (1999) *Eur. J. Phys. D* **5**, 193.
12 Drndić, M., Zabow, G., Lee, C.S., Thywissen, J.H., Johnson, K.S., Prentiss, M., Westervelt, R.M., Featonby, P.D., Savalli, V., Cognet, L., Helmerson, K., Westbrook, N., Westbrook, C.I., Phillips, W.D., and Aspect, A. (1999) *Phys. Rev. A* **60**, 4012.
13 Folman, R., Krüger, P., Schmiedmayer, J., Denschlag, J., and Henkel, C. (2002) *Adv. At., Mol. Opt. Phys.* **48**, 263.
14 Reichel, J. (2002) *Appl. Phys. B* **75**, 469.
15 Fortágh, J. and Zimmermann, C. (2007) *Rev. Mod. Phys.* **79**, 235.
16 Weinstein, J.D. and Libbrecht, K.G. (1995) *Phys. Rev. A* **52**, 4004.
17 Vuletić, V., Fischer, T., Praeger, M., Hänsch, T.W., and Zimmermann, C. (1998) *Phys. Rev. Lett.* **80**, 1634.
18 Fortágh, J., Grossmann, A., Zimmermann, C. and Hänsch, T.W. (1998) *Phys. Rev. Lett.* **81**, 5310.
19 Drndić, M., Johnson, K.S., Thywissen, J.H., Prentiss, M., and Westervelt, R.M. (1998) *Appl. Phys. Lett.* **72**, 2906.
20 Reichel, J., Hänsel, W., and Hänsch, T.W. (1999) *Phys. Rev. Lett.* **83**, 3398.
21 Denschlag, J., Cassettari, D., and Schmiedmayer, J. (1999) *Phys. Rev. Lett.* **82**, 2014.
22 Müller, D., Anderson, D.Z., Grow, R.J., Schwindt, P.D.D., and Cornell, E.A. (1999) *Phys. Rev. Lett.* **83**, 5194.
23 Dekker, N.H., Lee, C.S., Lorent, V., Thywissen, J.H., Smith, S.P., Drndić, M., Westervelt, R.M., and Prentiss, M. (2000) *Phys. Rev. Lett.* **84**, 1124.
24 Key, M., Hughes, I.G., Rooijakkers, W., Sauer, B.E., Hinds, E.A., Richardson, D.J., and Kazansky, P.G. (2000) *Phys. Rev. Lett.* **84**, 1371.
25 Davis, T.J. (1999) *J. Phys. B: Quant. Semicl. Opt.* **1**, 408.
26 Folman, R., Krüger, P., Cassettari, D., Hessmo, B., Maier, T., and Schmiedmayer, J. (2000) *Phys. Rev. Lett.* **84**, 4749.
27 Hänsel, W., Reichel, J., Hommelhoff, P., and Hänsch, T.W. (2001) *Phys. Rev. Lett.* **86**, 608.
28 Hänsel, W., Hommelhoff, P., Hänsch, T.W., and Reichel, J. (2001) *Nature* **413**, 498.

29 Ott, H., Fortágh, J., Schlotterbeck, G., Grossmann, A., and Zimmermann, C. (2001) *Phys. Rev. Lett.* **87**, 230401.

30 Aubin, S., Myrskog, S., Extavour, M.H.T., LeBlanc, L.J., McKay, D., Stummer, A., and Thywissen, J.H. (2006) *Nature Phys.* **2**, 384.

31 Treutlein, P., Hommelhoff, P., Steinmetz, T., Hänsch, T.W., and Reichel, J. (2004) *Phys. Rev. Lett.* **92**, 203005.

32 Knappe, S., Shah, V., Schwindt, P.D.D., Hollberg, L., Kitching, J., Liew, L.-A., and Moreland, J. (2004) *Appl. Phys. Lett.* **85**, 1460.

33 Shin, Y., Sanner, C., Jo, G.-B., Pasquini, T.A., Saba, M., Ketterle, W., Pritchard, D.E., Vengalattore, M. and Prentiss, M. (2005) *Phys. Rev. A* **72**, 021604.

34 Schumm, T., Hofferberth, S., Andersson, L.M., Wildermuth, S., Groth, S., Bar-Joseph, I., Schmiedmayer, J., and Krüger, P. (2005) *Nature Phys.* **1**, 57.

35 Wang, Y.-J., Anderson, D.Z., Bright, V.M., Cornell, E.A., Diot, Q., Kishimoto, T., Prentiss, M., Saravanan, R.A., Segal, S.R., and Saijun, W. (2005) *Phys. Rev. Lett.* **94**, 090405.

36 Jo, G.-B., Shin, Y., Will, S., Pasquini, T.A., Saba, M., Ketterle, W., Pritchard, D.E., Vengalattore, M., and Prentiss, M. (2007) *Phys. Rev. Lett.* **98**, 030407.

37 Böhi, P., Riedel, M.F., Hoffrogge, J., Reichel, J., Hänsch, T.W., and Treutlein, P. (2009) *Nature Phys.* **5**, 592.

38 Riedel, M.F., Böhl, P., Li, Y., Hänsch, T.W., Sinatra, A., and Treutlin, P. (2010) *Nature* **464**, 1170.

39 Deutsch, C. Ramirez-Martinez, F., Lacroûte, C., Reinhard, F., Schneider, T., Fuchs, J.N., Piéchon, F., Laloë, F., Reichel, J., and Rosenbusch, P. (2010) *Phys. Rev. Lett.* **105**, 020401.

40 Lhuiller, C. and Laloë, F. (1982) *J. Phys. (Paris)* **43**, 197 and 225.

41 Sinclair, C.D.J., Curtis, E.A., Llorente Garcia, I., Retter, J.A., Hall, B.V., Eriksson, S., Sauer, B.E., and Hinds, E.A. (2005) *Phys. Rev. A* **72**, 031603.

42 Hall, B.V., Whitlock, S., Scharnberg, F., Hannaford, P., and Sidorov, A. (2005) *Laser Spectroscopy 17*, (eds E.A. Hinds, A. Ferguson, and E. Riis), World Scientific, Singapore, p. 275.

43 Hall, B.V., Whitlock, S., Scharnberg, F., Hannaford, P., and Sidorov, A. (2006) *J. Phys. B* **39**, 27.

44 Boyd, M., Streed, E.W., Medley, P., Campbell, G.K., Mun, J., Ketterle, W., and Pritchard, D.E. (2007) *Phys. Rev. A* **76**, 043624.

45 Fernholz, T., Gerritsma, R., Whitlock, S., Barb, I., and Spreeuw, R.J.C. (2008) *Phys. Rev. A* **77**, 033409.

46 Gerritsma, R., Whitlock, S., Fernholz, T., Schlatter, H., Luigjes, J.A., Thiele, J.-U., Goedkoop, J.B., and Spreeuw, R.J.C. (2007) *Phys. Rev. A* **76**, 033408.

47 Whitlock, S., Fernholz, T., Gerritsma, R., Schlatter, H., Luigjes, J.A., Thiele, J.-U., Goedkoop, J.B., and Spreeuw, R.J.C. (2009) *New J. Phys.* **11**, 023021.

48 Singh, M., Whitlock, S., Anderson, R., Ghanbari, S., Hall, B.V., Volk, M., Akulshin, A., McLean, R., Sidorov, A., and Hannaford, P. (2008) *Laser Spectroscopy 18* (eds J. Bergquist, L. Hollberg, and M. Kasevich), New York, World Scientific, p. 228.

49 Singh, M., Volk, M., Akulshin, A., Sidorov, A., McLean, R., and Hannaford, P. (2008) *J. Phys. B* **41**, 065301.

50 Nirrengarten, T., Qarry, A., Roux, C., Emmert, A., Nogues, G., Brune, M., Raimond, J.-M., and Haroche, S. (2006) *Phys. Rev. Lett.* **97**, 200405.

51 Mukai, T., Hufnagel, C., Kasper, A., Meno, T., Tsukada, A., Semba, K., and Shimizu, F. (2007) *Phys. Rev. Lett.* **98**, 260407.

52 Roux, C., Emmert, A., Lupascu, A., Nirrengarten, T., Nogues, G., Brune, M., Raimond, J.-M., and Haroche, S. (2008) *Eur. Phys. Lett.* **81**, 56004.

53 Cano, D., Kasch, B., Hattermann, H., Kleiner, R., Zimmermann, C., Koelle, D., and Fortágh, J. (2008) *Phys. Rev. Lett.* **101**, 183006.

54 Singh, M. (2009) *Opt. Express* **17**, 2600.

55 Hinds, E.A. and Hughes, I.G. (1999) *J. Phys. D* **32**, R119.

56 Lau, D.C., McLean, R.J., Sidorov, A.I., Gough, D.S., Koperski, J., Rowlands, W.J., Sexton, B.A., Opat, G.I., and Hannaford, P. (1999) *J. Opt. B* **1**, 371.

57 Davis, T.J. (2001) *Eur. J. Phys. D* **14**, 111.

58 Opat, G.I., Nic Chormaic, S., Cantwell, B.P., and Richmond, J.A. (2004) *J. Opt. B* **1**, 415 (1999).

59 Wang, J.Y., Whitlock, S., Scharnberg, F., Gough, D.S., Sidorov, A.I., McLean, R.J., and Hannaford, P. (2005) *J. Phys. D* **38**, 4015.

60 Hinds, E.A., Boshier, M.G., and Hughes, I.G. (1998) *Phys. Rev. Lett.* **80**, 645.

61 Eriksson, S., Ramirez-Martinez, F., Curtis, E.A., Sauer, B.E., Nutter, P.W., Hill, E.W., and Hinds, E.A. (2004) *Appl. Phys. B* **79**, 811.

62 Krüger, P., Luo, X., Klein, M.W., Brugger, K., Haase, A., Wildermuth, S., Groth, S., Bar-Joseph, I., Folman, R., and Schmiedmayer, J. (2003) *Phys. Rev. Lett.* **91**, 233201.

63 Henkel, C., Pötting, S., and Wilkins, M. (1999) *Appl. Phys. B* **69**, 379.

64 Whitlock, S. (2007) *Bose–Einstein condensates on a magnetic film atom chip* PhD thesis, Swinburne University of Technology, p. 92.

65 Fortágh, J., Ott, H., Kraft, S., Günther, A., and Zimmermann, C. (2002) *Phys. Rev. A* **66**, 041604.

66 Whitlock, S., Hall, B.V., Roach, T., Anderson, R., Volk, M., Hannaford, P., and Sidorov, A. (2007) *Phys. Rev. A* **75**, 043602.

67 Wildermuth, S., Hofferberth, S., Lesanovsky, I., Haller, E., Andersson, L.M., Groth, S., Bar-Joseph, I., Krüger, P., and Schmiedmayer, J. (2005) *Nature* **435**, 440.

68 Luiten, O.J., Reynolds, M.W., and Walraven, J.T.M. (1996) *Phys. Rev. A* **53**, 381.

69 Wang, D.W., Lukin, M.D., and Demler, E. (2004) *Phys. Rev. Lett.* **92**, 076802.

70 Estéve, J., Aussibal, C., Schumm, T., Figl, C., Mailly, D., Bouchoule, I., Westbrook, C.I., and Aspect, A. (2004) *Phys. Rev. A* **70**, 043629.

71 Hall, B.V., Whitlock, S., Anderson, R., Hannaford, P., and Sidorov, A. (2007) *Phys. Rev. Lett.* **98**, 030402.

72 McGuirk, J.M., Foster, G.T., Fixler, J.B., Snaddon, M.J., and Kasevich, M.A. (2002) *Phys. Rev. A* **65**, 033608.

73 Anderson, R.P., Ticknor, C., Sidorov, A.I., and Hall, B.V. (2009) *Phys. Rev. A* **80**, 023603.

74 Mertes, K.M., Merrill, J.W., Carretero-Gonzáles, R., Frantzeskakis, D.J., Kevrekidis, P.G., and Hall, D.S. (2007) *Phys. Rev. Lett.* **99**, 190402.

75 For example, Bloch, I. (2004) *Physics World* **98**(4), 25.

76 Tolra Laburthe, B., O'Hara, K.M., Huckans, J.H., Phillips, W.D., Rolston, S.L., and Porto, J.V. (2004) *Phys. Rev. Lett.* **92**, 19040.

77 Kinoshita, T., Wenger, T., and Weiss, D.S. (2006) *Nature* **440**, 900.

78 Greiner, M., Mandel, O., Esslinger, T., Hänsch, T., and Bloch, I. (2002) *Nature* **415**, 39.

79 Billy, J., Josse, V., Zuo, Z., Bernard, A., Hambrecht, B., Lugan, P., Clement, D., Sanchez-Palencia, L., Bouyer, P., and Aspect, A. (2008) *Nature* **453**, 891.

80 Roati, G., D'Errico, C., Fallani, L., Fattori, M., Fort, C., Zaccanti, M., Modugno, G., Modugno, M., and Inguscio, M. (2008) *Nature* **453**, 895.

81 Calarco, T., Hinds, E.A., Jaksch, D., Schmiedmayer, J., Cirac, J.I., and Zoller, P. (2000) *Phys. Rev. A* **61**, 022304.

82 Schrader, D., Dotsenko, I., Khudaverdyan, M., Miroshnychenko, Y., Rauschenbeutal, A., and Meschede, D. (2004) *Phys. Rev. Lett.* **93**, 150501.

83 Ghanbari, S., Kieu, T.D., Sidorov, A., and Hannaford, P. (2006) *J. Phys. B* **39**, 847.

84 Ghanbari, S., Kieu, T.D., and Hannaford, P. (2007) *J. Phys. B* **40**, 1283.

85 Günther, A., Kemmler, M., Kraft, S., Vale, C.J., Zimmermann, C., and Fortágh, J. (2005) *Phys. Rev. A* **71**, 063619.

86 Sinclair, D.J., Retter, J.A., Curtis, E.A., Hall, B.V., Llorente Garcia, I., Eriksson, S., Sauer, B.E., and Hinds, E.A. (2005) *Eur. Phys. J.* **35**, 105.

87 Yin, J., Gao, W., Hu, J., and Wang, Y. (2002) *Opt. Commun.* **206**, 99.

88 Grabowski, A. and Pfau, T. (2003) *Eur. Phys. J. D* **22**, 347.

89 Jose, S., Krzemien, L., Withlock, S., Singh, M., Sidorov, A., McLean, R., and Hannaford, P. *In preparation.*